Supporting information

The octahedral distortion promotes the dynamic reconstruction for enhanced water oxidation

Jing Qi,*[a] Yajing Zhao,[a] Ying Gao,[a] Jing Li,[b] Shengbo Gao[a] and Mingxing Chen*[a]

[a]School of Materials Science and Engineering, Henan Normal University, Xinxiang 453007, China
[b]School of Chemistry and Chemical Engineering, Henan Normal University, Xinxiang 453007, China

Experimental Section

Materials

$Co(NO_3)_2 \cdot 6H_2O$ (98%, Anhui Senrise Technologies Co.), $K_4P_2O_7$ (99%, Anhui Senrise Technologies Co.), KOH (98%, Sinopharm Chemicals), $NH_4H_2PO_4$ (99%, Aladdin Reagent), Nafion solution (5 wt%, DuPont), H_3PO_4 (≥85%, Sigma-Aldrich), KNO_3 (99%, Chengdu Kelong Chemicals Co.), CH_3CH_2OH (99.5%, Sigma-Aldrich) and $CO(NH_2)_2$ (99.5%, Energy Chemical) were obtained from commercial suppliers without further purification. All solutions were prepared with Milli-Q water (18 MΩ cm).

Synthesis of $K_2Co_3(P_2O_7)_2$

$Co(NO_3)_2 \cdot 6H_2O$ (0.5 mmol) was dissolved in 20 mL of C_2H_5OH at room temperature under stirring. $K_4P_2O_7$ (1 mmol) was dissolved in 20 mL of deionized water, and then added to the cobalt alcohol solution. The obtained mixture was stirred for 30 min. Subsequently, 65 uL of H_3PO_4 was added into the mixture. The resulting suspension was stirred at 70 °C for 3.5 h. The product was collected by centrifugation, washed with deionized water and ethanol, and dried in an oven at 60 °C.

Synthesis of $KCo(PO_3)_3$

KNO_3 (2 mmol), $Co(NO_3)_2 \cdot 6H_2O$ (1 mmol), $NH_4H_2PO_4$ (4 mmol) and $CO(NH_2)_2$ (1 mmol) were added to 15 mL of deionized water and stirred for 30 min. Then, the resulting suspension was stirred at 90 °C until complete evaporation of water. The solid was calcined in air at 350 °C for 30 min to obtain potassium cobalt trimetaphosphate.

Physical characterization

X-ray diffraction (XRD) data were acquired on a Bruker D8 Advance diffractometer with Cu Kα radiation. Ultraviolet-visible diffuse reflectance spectra (400-1000 nm) of solid samples were recorded on a Shimadzu UV 3600 spectrophotometer. Scanning electron microscopy (SEM, SUPRA40, Zeiss) was used to observe the surface morphology. X-ray photoelectron spectroscopy (XPS) data were obtained with a Thermo Scientific Escalab 250Xi electron spectrometer using Al-Kα radiation (hν = 1486.6 eV). Magnetic measurements were performed on a physical property measurement system (PPMS, VersaLab, Quantum Design). *In situ* Raman spectra were recorded on a LabRAM Raman microscope (LabRAM Odyssey Nano, Horiba) using a 532 nm laser.

Electrochemical measurement

All electrochemical tests were performed using a CHI660E electrochemical workstation. A three-electrode system was employed, with a glassy carbon working electrode (GC, 0.07 cm^2), a saturated Ag/AgCl reference electrode and a graphite rod counter electrode. The catalyst ink

was prepared by dispersing 4 mg of sample in 1.0 mL of deionized water and 30 μL of Nafion under ultrasonication for 30 min. Subsequently, 5 μL of the catalyst ink was loaded onto the GC electrode and dried at room temperature. An alkaline 1.0 M KOH (pH = 13.8) solution was used as the electrolyte. All measured potentials were reported against the reversible hydrogen electrode (RHE) by using the equation $E_{RHE} = E_{Ag/AgCl} + 0.059 \times pH + 0.197$. Linear sweep voltammetry (LSV) and cyclic voltammetry (CV) measurements were performed at scan rates of 5 and 50 mV s^{-1}, respectively, with 100% iR compensation. The Tafel slope was determined by plotting the OER overpotential against the logarithm of the current density. Differential pulse voltammetry (DPV) curves were recorded at an amplitude of 50 mV with 100% iR compensation. *Operando* electrochemical impedance spectroscopy (EIS) was carried out at various potentials over a frequency range from 0.01 to 100000 Hz with an amplitude of 5 mV. The stability test was evaluated by chronopotentiometry at a current density of 10 mA cm^{-2} without iR drop compensation. Fourier-transformed alternating current voltammetry (FTacV) data was obtained using an amplitude of 160 mV and a frequency of 9 Hz.

Equation S1:

$$\Delta = \frac{1}{N}\sum_{k=1}^{N}\frac{|d_k - d_m|}{d_m}$$

where d_k, d_m, and N represent the Co-O bond length, the average Co-O bond length and the number of Co-O bonds per polyhedron, respectively.

Equation S2:

$$\mu_{eff} = \sqrt{8C}\mu_B = 2.828\sqrt{\chi_m T} = \sqrt{n(n+2)}$$

where μ_{eff} and n represent the effective paramagnetic moment and the number of unpaired electrons, respectively. The magnetic susceptibilities $\chi = \frac{M}{H}$, in which M and H represent magnetization and magnetic field, respectively. Moreover, the χ under high temperature follows the paramagnetic Curie-Weiss law: $\chi = \frac{C}{(T - T_\theta)}$, in which C and T_θ represent the Curie constant and Curie-Weiss temperature, respectively. The C is calculated by fitting the temperature-dependent magnetic susceptibility (χ) in the high-temperature region.

Equation S3:

$$TOF = \frac{i \times S}{4nF}$$

where i and S represent the measured current and geometric area, respectively.

Equation S4:

$$E_c = E_{1/2} - \left(\frac{RT}{\alpha nF}\right) \times \ln\left(\frac{\alpha nF}{RTk_s}\right) - \left(\frac{RT}{\alpha nF}\right) \times \ln v$$

where k_s, v, n and α represent the rate constant, scan rate, number of electrons and transfer coefficient, respectively. E_c and $E_{1/2}$ represent the reduction and formal potentials of the cobalt redox.

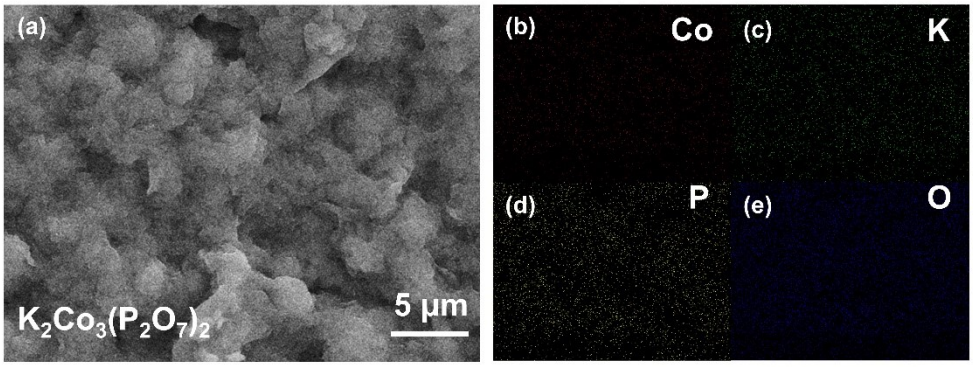

Fig. S1 The SEM image (a) and the corresponding elemental mapping images (b-e) of $K_2Co_3(P_2O_7)_2$.

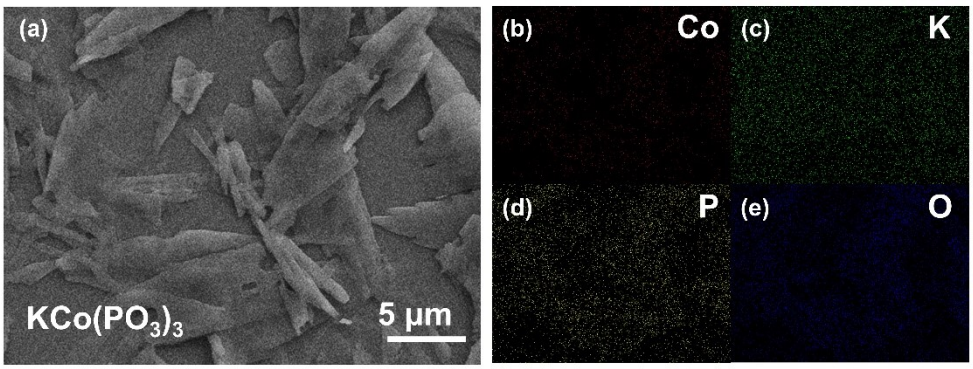

Fig. S2 The SEM image (a) and the corresponding elemental mapping images (b-e) of $KCo(PO_3)_3$.

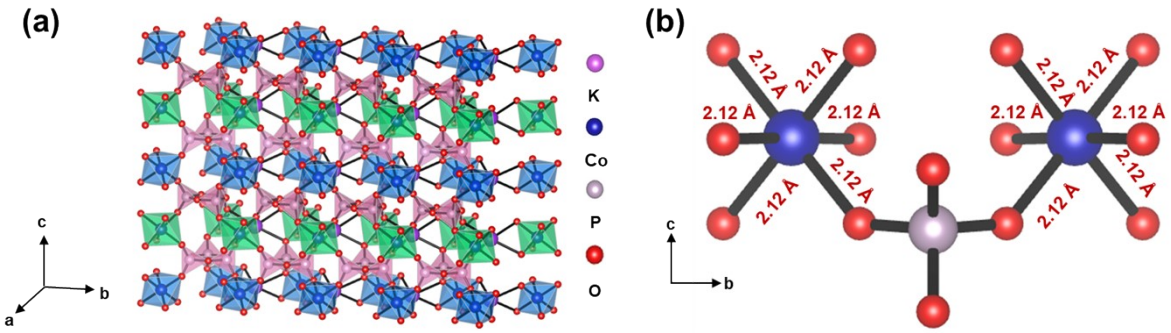

Fig. S3 (a) Crystal structure of $KCo(PO_3)_3$ and (b) the corresponding Co-O bonds length.

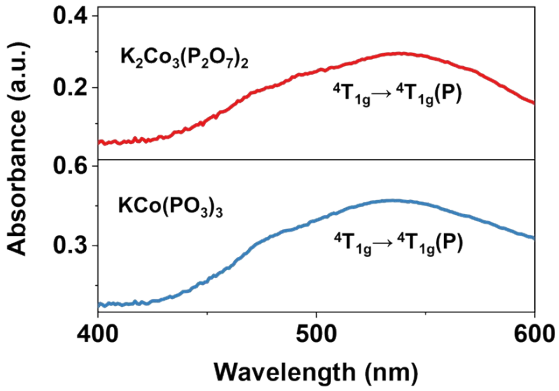

Fig. S4 UV-vis spectra of the $K_2Co_3(P_2O_7)_2$ and $KCo(PO_3)_3$ samples.

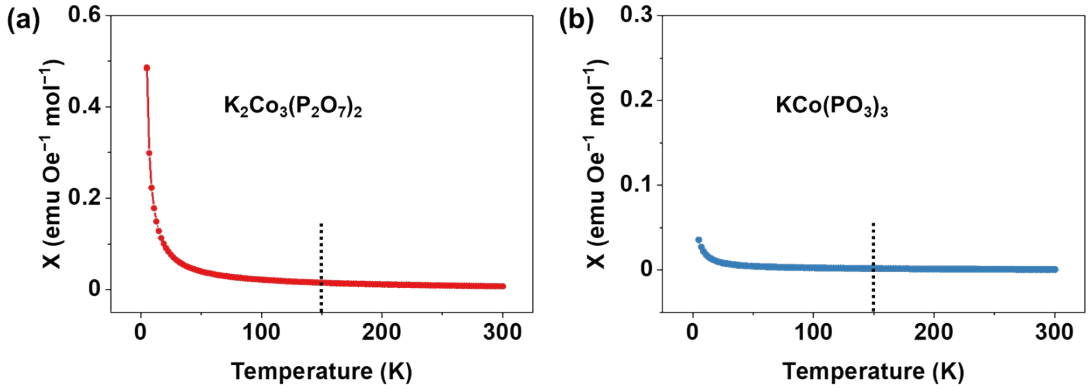

Fig. S5 The magnified temperature-dependent magnetic susceptibility curves of (a) $K_2Co_3(P_2O_7)_2$ and (b) $KCo(PO_3)_3$ at 1000 Oe.

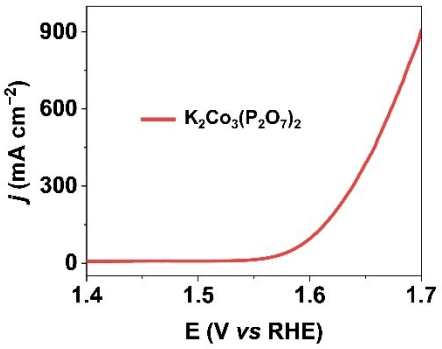

Fig. S6 The LSV curve of $K_2Co_3(P_2O_7)_2$ on a carbon cloth electrode in 1 M KOH.

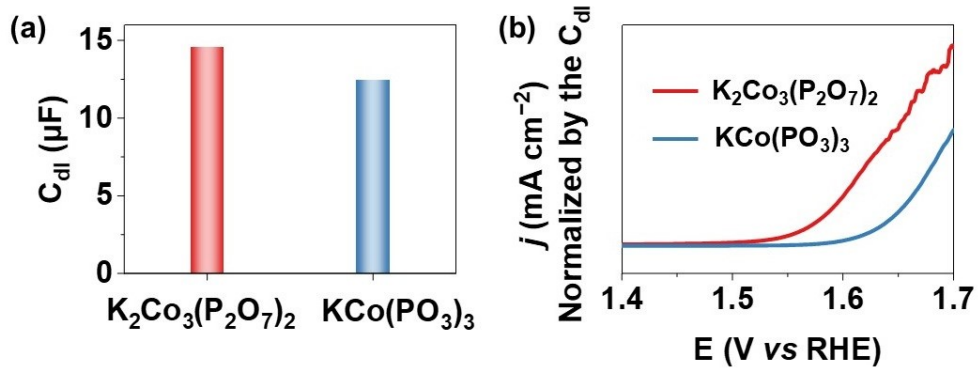

Fig. S7 (a) The double-layer capacitance of $K_2Co_3(P_2O_7)_2$ and $KCo(PO_3)_3$ calculated from EIS plots. (b) The current densities normalized by the C_{dl} of $K_2Co_3(P_2O_7)_2$ and $KCo(PO_3)_3$.

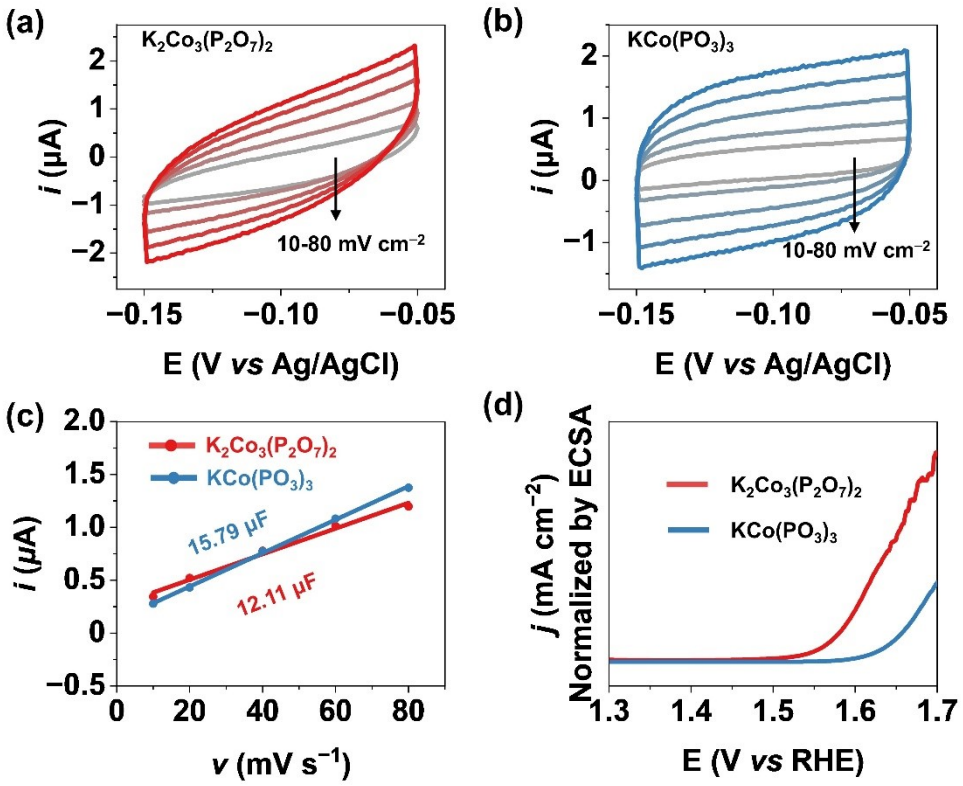

Fig. S8 CV curves of the reconstructed (a) $K_2Co_3(P_2O_7)_2$ and (b) $KCo(PO_3)_3$ acquired in the non-Faradaic potential range (−150~50 mV *vs* Ag/AgCl) at different scan rates (10-80 mVs^{-1}) in 1.0 M KOH solutions. (c) The surface capacitance values of $K_2Co_3(P_2O_7)_2$ and $KCo(PO_3)_3$. (d) The current densities normalized by the ECSAs of $K_2Co_3(P_2O_7)_2$ and $KCo(PO_3)_3$.

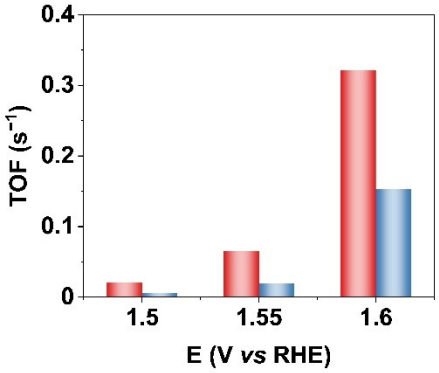

Fig. S9 TOF values of $K_2Co_3(P_2O_7)_2$ and $KCo(PO_3)_3$ calculated from the oxidation peak areas.

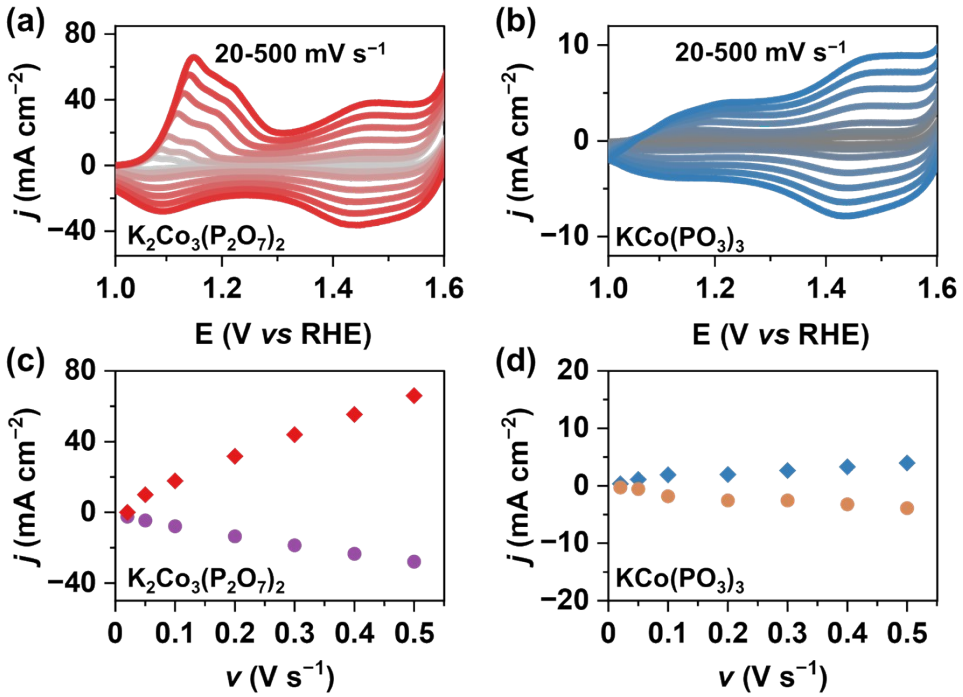

Fig. S10 CV curves of (a) $K_2Co_3(P_2O_7)_2$ and (b) $KCo(PO_3)_3$ at different scan rates (20, 50, 100, 200, 300, 400, and 500 mV s^{-1}). The peak currents plotted against the scan rates for (c) $K_2Co_3(P_2O_7)_2$ and (d) $KCo(PO_3)_3$.

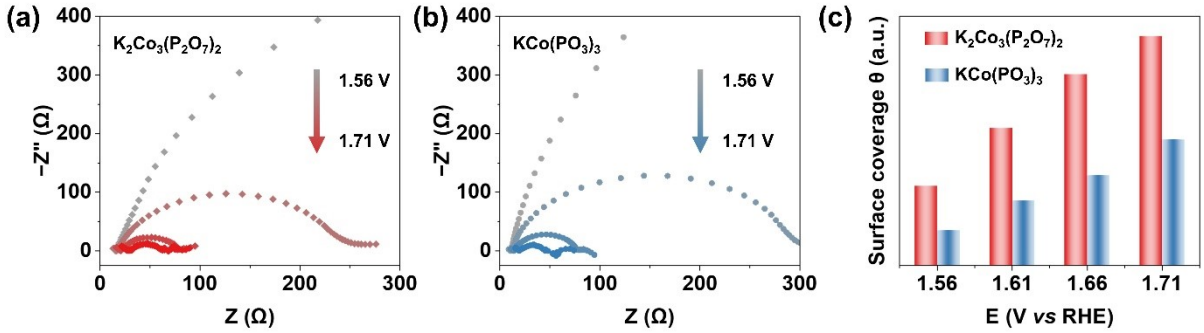

Fig. S11 EIS plots of (a) $K_2Co_3(P_2O_7)_2$ and (b) $KCo(PO_3)_3$ at different potentials (1.56, 1.61, 1.66, 1.71 V). (c) Surface coverage of oxygenated intermediates of $K_2Co_3(P_2O_7)_2$ and $KCo(PO_3)_3$ calculated from EIS plots.

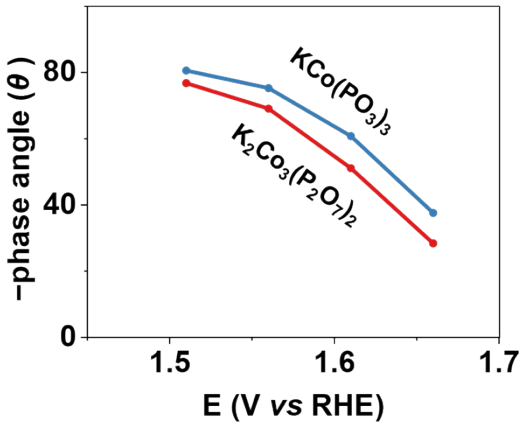

Fig. S12 The phase peak angles of $K_2Co_3(P_2O_7)_2$ and $KCo(PO_3)_3$ from 1.51 to 1.66 V.

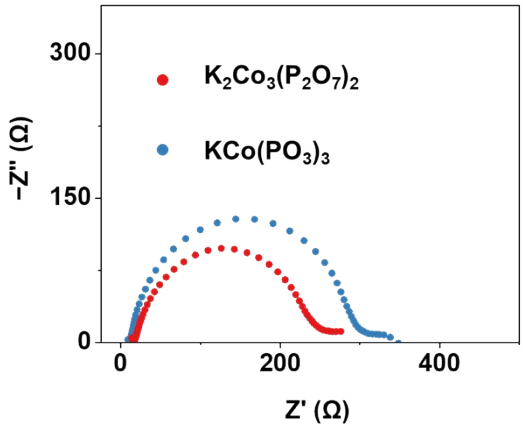

Fig. S13 The Nyquist plots of $K_2Co_3(P_2O_7)_2$ and $KCo(PO_3)_3$ at 1.61 V.

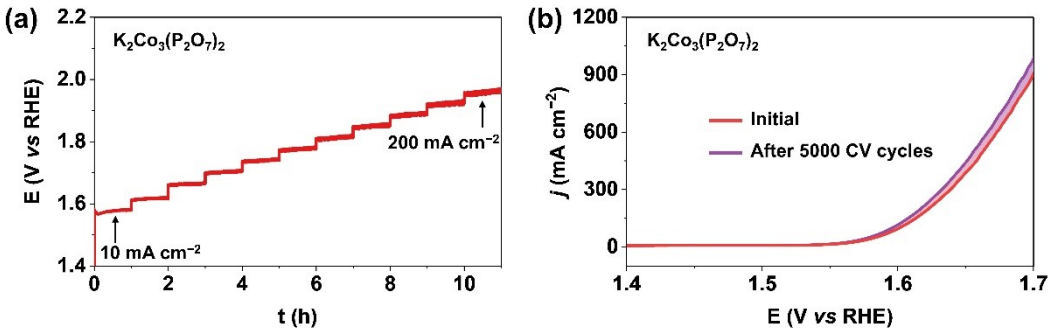

Fig. S14 (a) Multi-step current curves of $K_2Co_3(P_2O_7)_2$ in 1 M KOH. (b) LSV curves of $K_2Co_3(P_2O_7)_2$ before and after 5000 CV cycles.

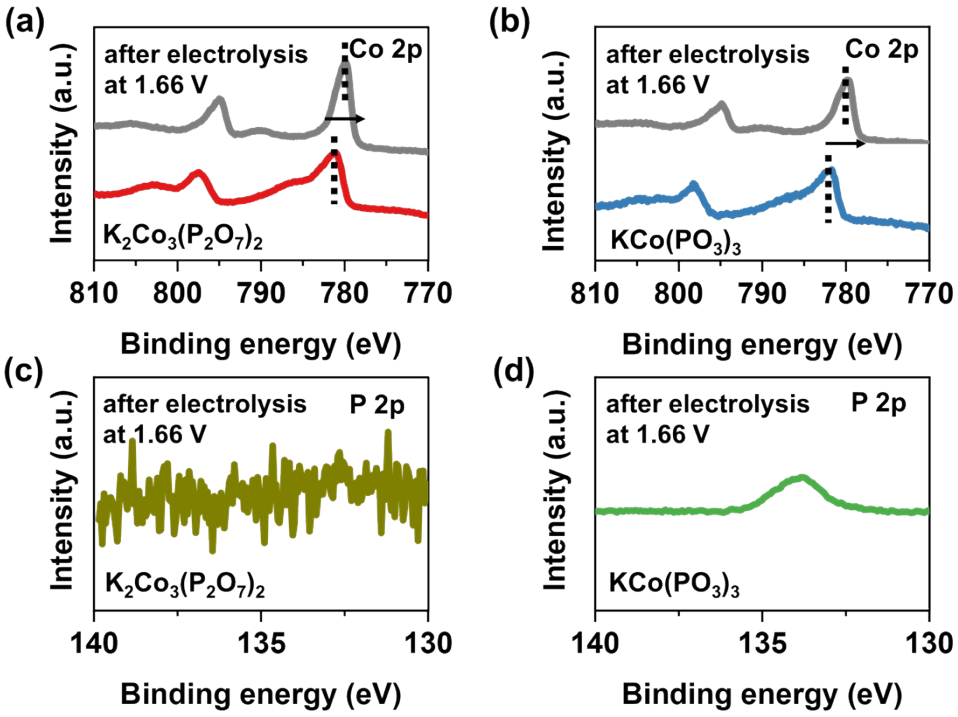

Fig. S15 XPS spectra of (a, b) Co 2p and (c, d) P 2p for $K_2Co_3(P_2O_7)_2$ and $KCo(PO_3)_3$ after OER electrolysis.

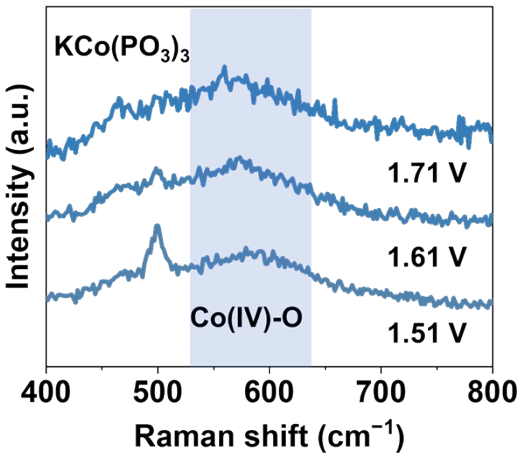

Fig. S16 *In situ* Raman spectra of $KCo(PO_3)_3$ from 1.51 V to 1.71 V.

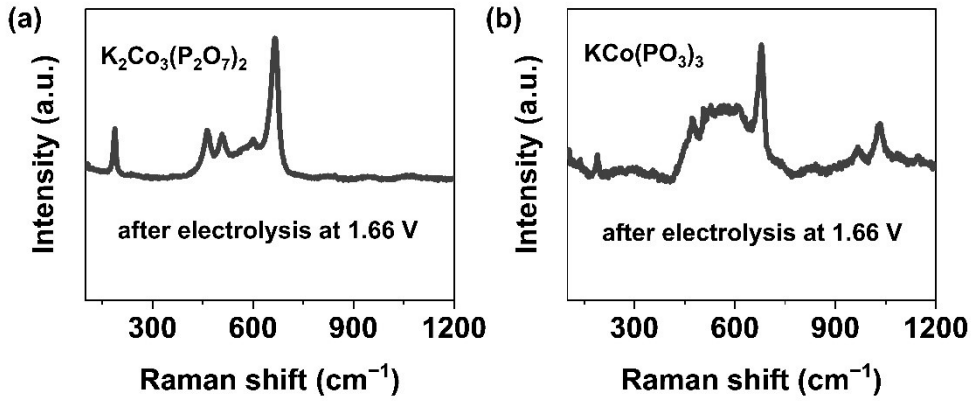

Fig. S17 Raman spectra of (a) $K_2Co_3(P_2O_7)_2$ and (b) $KCo(PO_3)_3$ after electrolysis.

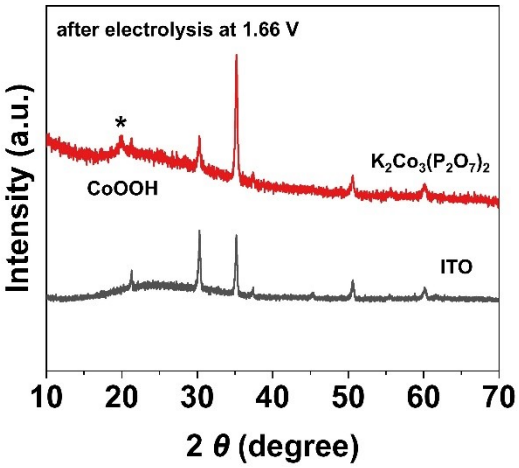

Fig. S18 XRD patterns of blank indium tin oxide (ITO) and post-electrolysis $K_2Co_3(P_2O_7)_2$.

Table S1 Comparison of OER performance of $K_2Co_3(P_2O_7)_2$ with other reported transition metal-based materials.

Catalyst	Substrate	Electrolyte	Overpotential @10 mA cm^{-2} (mV)	Reference
$K_2Co_3(P_2O_7)_2$	**GC**	**1 M KOH**	**339**	**This work**
$KCo(PO_3)_3$	**GC**	**1 M KOH**	**400**	**This work**
AP-$CoMoO_4$	NF	1 M KOH	328	*Energy Environ. Mater.*, **2024**, *7*, e12495.
$Co(OH)_2$-CeO_2	CP	1 M KOH	329.6	*Chem. Commun.*, **2026**, *62*, 946.
$Co_{11}(HPO_3)_8(OH)_6$	GC	1 M KOH	340	*Appl. Catal. B Environ.*, **2019**, *259*, 118091.
$Co_2P_2O_7$ nanowires	GC	1 M KOH	359	*Small*, **2018**, *14*, 1801068.
CoFe-N-C	GC	1 M KOH	360	*Nano Lett.*, **2022**, *22*, 3392.
CoFeO NMs	NF	1 M KOH	310	*Electrochim. Acta*, **2021**, *368*, 137651.
$Na_2Co_{0.75}Fe_{0.25}P_2O_7$/C	Rotating disk electrode	0.1 M KOH	300	*ACS Catal.*, **2020**, *10*, 702.
Co@CoFe-O	GC	1 M KOH	342	*Energy Environ. Sci.,* **2022**, *15*, 727.
$NiCo_2O_4$ NBs	CP	1 M KOH	330	*Angew. Chem. Int. Ed.*, **2021**, *60*, 11841.
$Na_{0.75}CoO_2$	GC	1 M NaOH	370	*Chem. Mater.*, **2021**, *33*, 6299.